Nezha-F: Design and Analysis of a Foldable and Self-Deployable HAUV

Yulin Bai, Yufei Jin, Chunhu Liu, Zheng Zeng and Lian Lian

***Abstract*— This paper introduces a small hybrid aerial underwater vehicle (HAUV), which we named Nezha-F, that can fly in the air, perform vertical profiling underwater, and vertically take off and land from both the water surface and ground. A foldable and self-deployable arm mechanism linked to and driven by a piston variable buoyancy system (PVBS) is proposed to reduce the excessive underwater drag caused by aerial structures. By having a compact size and successfully balanced aerial and underwater performance without adding excessive actuators, this design provides a feasible idea for the miniaturization of amphibious floats. The dynamic characteristics of the small PVBS are linear fitted, and modeled. The originally nonlinear actuator performance is linearized by the post-fitting mapping. Asymmetric dead zones of the actuator are removed by adding compensation to the algorithm. During a 10-day field test, the vehicle showed good aerial performance and underwater control effect. Several full mission cycle tests proved the vehicle's ability in semi-autonomous operation and robust domain crossing and verified the vehicle's endurance during each mission stage.**

***Index Terms*— Hybrid aerial underwater vehicle, Piston variable buoyancy system, Arm foldable mechanism**

I. INTRODUCTION

Joint observations of water and air are crucial for studying physical phenomena on the ocean's surface. With the maturity of unmanned aerial vehicles (UAV), more and more traditional unmanned underwater vehicles (UUV) are combined with UAV, integrating the original two sets of observation equipment on one platform [1]. The traditional fixed-wing UAV can realize the water-air cross-domain process after the electronic cabin is sealed and the water-permeable wing is replaced [2]. Nezha III combines UAV and glider to realize the functions of underwater zigzag observation and aerial cruise [3]. The combination of the UAV and autonomous underwater vehicles (AUV) enables the vehicle to have strong maneuverability in the air and underwater [4]. In addition, miniaturized hybrid aerial underwater vehicle (HAUV) airframes have also received great attention in the past time due to their easy clustering, high maneuverability, and stealth characteristics [5].

Due to the obvious difference between the two media, water and air, the traditional configuration originally in one medium is not suitable for the other medium. Usually the shape of the underwater vehicle is streamlined. This can effectively reduce the pressure drag and vortex generated by the vehicle when navigating through the water. By reducing damping, power consumption is reduced, and maneuverability is improved so that the underwater vehicle can normally work underwater for a long time [6]. Most multi-rotors HAUV are not streamlined due to their outward extending arms and motors, which cause more drag when moving underwater. So they are unsuitable for direct underwater use. Finding a mechanical solution that can change the vehicle's shape is the key to the design of amphibious vehicles.

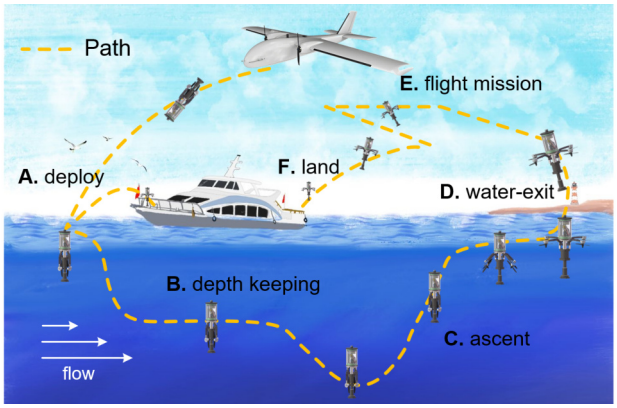

Fig. 1. Schematic diagram of working mode

The shape of the folding arm has been widely used in UAV [7]. This structure makes the vehicle more convenient to carry and has advantages in traversing narrow spaces [8] and broadening the launch scene [9,10]. However, they have the disadvantages of not being able to fold actively, requiring additional motor drive, and being unable to fold repeatedly. The concept of foldable fixed wings in HAUV has long been proposed [11], and Dipper [12] recently completed field tests. But fixed-wing HAUV is more affected by the disturbance when crossing the water surface, and the success rate is lower than that in the quadrotor configuration. Moreover, fixed-wing HAUV miniaturization is also more difficult due to the need for wings large enough to provide lift. A multi-rotor HAUV with motor-driven foldable arms has been developed [3], but this structure is not conducive to the miniaturization and light weight of the body. The HAUV presented in [13] uses a coaxial counter-propeller-tilting platform with foldable blades to achieve a streamlined shape.

Float is an ocean observation device that can actively change its buoyancy to achieve vertical movement in the ocean. Compared with other underwater vehicles, the float has the unique advantages of hovering at a fixed depth, following the water flow, and lowering power consumption [14]. Combining it with UAV can compensate for poor

This work was supported in part by the National Natural Science Foundation of China under Grant 41706108, in part by the Shanghai Committee Science and Technology under Project 20dz1206600, in part by the Natural Science Foundation of Shanghai under Grant 20ZR1424800, and in part by the Shanghai Jiao Tong University Scientific and Technological Innovation Funds under Grant 2019QYB04. (Corresponding author: Zheng Zeng.)

The authors are with the School of Oceanography, Shanghai Jiao Tong University, Shanghai, Minhang District 200240, China (e-mail: bylsjtu@sjtu.edu.cn; zheng.zeng@sjtu.edu.cn; llian@sjtu.edu.cn).

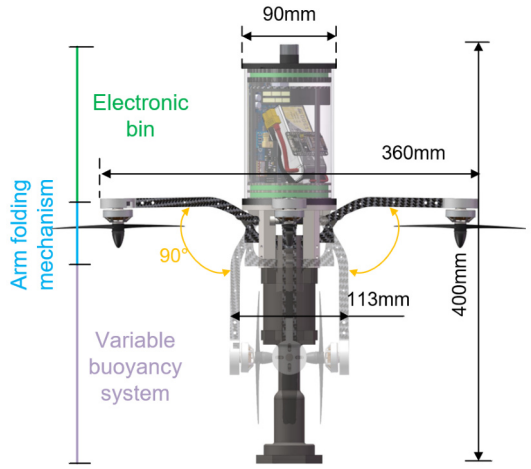

Fig. 2. Overall schematic diagram and key position dimensions

maneuverability shortcomings and be applied to special observation scenarios. The variable buoyancy system used on traditional floats can be divided into piston type [15] and oil pumping type [16]. The piston-type VBS commonly used on floats has the advantages of small size, simple structure, and low power consumption [15]. More importantly, while changing the buoyancy, it can also naturally act as a drive unit for the opening and closing of the arm. It provides the possibility for the miniaturization of amphibious float. Therefore, this paper adopts the PVBS. Table I shows the current performance of several different types of HAUV. It can be found that vehicles with VBS have disadvantages in weight and size. In addition, subsea thrusters generally have greater underwater maneuverability than VBS. But underwater vehicles driven by thrusters need to overcome static buoyancy all the time to do work. Therefore, the underwater endurance of HAUV containing VBS is generally higher than that without VBS.

This paper reports a new type of HAUV with foldable and self-deployable arms, which we named Nezha-F. Fig. 1 shows the working scenario of Nezha-F. The Nezha-F can be deployed by airdrop or fly to the target on its own from the deck or shore. It has active movement in the vertical direction and is capable of hovering at a certain depth for long periods of time. Horizontally it can drift with the current. After performing an underwater mission, it can cross the surface and return on its own. PVBS and foldable arm mechanism are integrated through the unique crank slider structure, giving Nezha-F a more streamlined underwater shape. The effect of such a structure in reducing power consumption is carried out. In addition, the PVBS

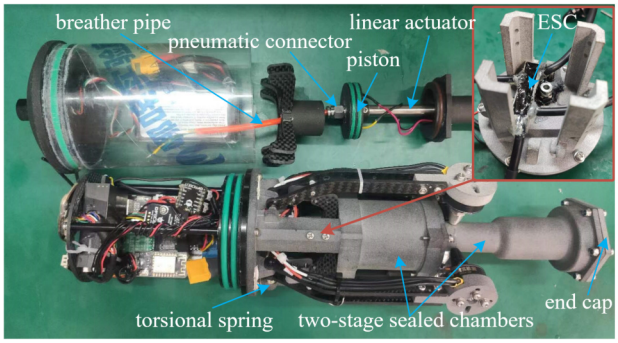

Fig. 3. Physical assembly drawing and detail display

used by Nezha-F is accurately modeled by pre-experiments. A control compensation method for the PVBS is proposed to improve the dynamic performance of Nezha-F underwater. Through field tests, the full mission capability of Nezha-F is verified, and its performance is consistent with the simulation analysis.

II. PROTOTYPE VEHICLE DESIGN

The whole body will be divided into three parts: variable buoyancy system (VBS), arm foldable mechanism, and electronic bin, as shown in Fig. 2.

A. Variable Buoyancy System

As shown in Fig. 3, the PVBS consists of a bidirectional variable-speed linear actuator, a piston, two-stage sealed chambers, and a sealed end cap. O-rings are used to seal the joints of all components. The thrust of the linear actuator can reach 180N, and the stroke is 50mm. The pushing speed of the actuator can be controlled by the voltage of 0-12v, and the maximum pushing speed is 5mm/s. The final PVBS can be adjusted to a maximum volume of 69 ml.

It is worth noting that when the piston is pushed out, negative pressure will be created in the cavity of the PVBS, which will increase the power consumption and reduce the deepest depth that the vehicle can dive. According to Boyle's law, increasing the initial volume can weaken this negative effect. Eventually, the PVBS is connected to the electronic compartment by adding a pneumatic plug and breather pipe. As shown in Fig. 3. This allows the gas to be connected between the VBS and the electronic bin, resulting in a larger initial volume of the enclosed space.

And Fig. 4 shows the power consumption of the PVBS before and after the optimization. The experimental scenario is to complete the conversion between maximum and minimum buoyancy at a depth of 0m with a voltage of 12V.

TABLE I
COMPARISON OF THE STRUCTURE AND PERFORMANCE OF SEVERAL HAUVS

Name	Type	VBS	Weight	Minimum size	Air endurance	Water endurance
Dipper[12]	foldable fix-wing	×	3.1kg	0.4×1.16m	4min	8min
Looncopter[17]	quadrotor	✓	2.7kg	>500mm	10.5-12min	11h/22min
Morphable HAUV[4]	quadrotor	×	505g	380mm	7min	<2.2h
Nezha-mini[5]	quadrotor	×	953g	280×193×91mm	4min	≈2h
Nezha-F	foldable quadrotor	✓	1.25kg	113×400mm	4min41s	29.54h

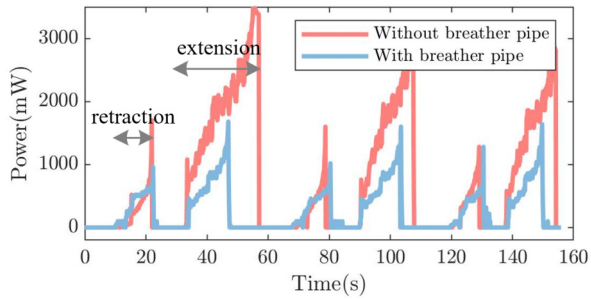

Fig. 4. Effect of breather pipe on power consumption of PVBS

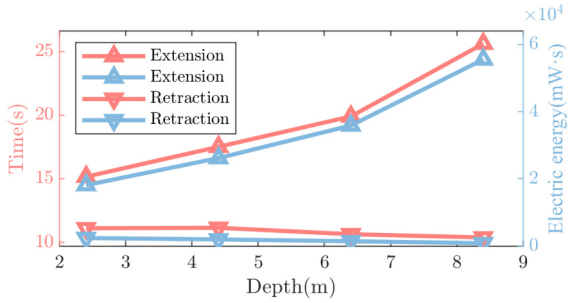

Fig. 5. PVBS performance with depth (At standard voltage of 12V).

1) It can be seen from Fig. 4 that the structure with a breather pipe has smaller peak power, shorter time, and lower total power consumption in the extension stage. During the retraction process, the structure before optimization allows a greater negative pressure in the VBS, which can offset part of the effect of friction. Therefore, the overall power consumption and time during retraction are slightly shorter. After optimization, the average power consumption is reduced by 66%, and 6.25s shorten the average deployment time.
2) Whether optimized or not, the retraction and extension times are different. This difference is more obvious in the vehicle without a breather pipe. It can be preliminarily inferred that the dynamic performance of the linear actuator deteriorates with the increase of depth.

Fig. 5 shows the time and power consumption for the piston rod to be fully extended and fully retracted at different depths. By placing Nezha-F in a leak test apparatus filled with water and applying different levels of pressure to simulate different water depths. The movement of the piston can be achieved by sending the relevant command via the serial port at the corresponding depth. The data are the average of three repeated experiments. With increasing depth (pressure), the linear actuator extension time shows a nonlinear increase. However, the retraction time is almost the same. In addition, the power consumption of the linear actuator operation is related to both time and depth. At the same time, conclusion 2) is also verified. A detailed solution to this problem will be given later.

B. Arm Foldable and Self-deployable Mechanism

To not introduce a new driving mechanism, this paper proposes a novel semi-linked foldable and self-deployable arm structure combined with the PVBS. By introducing the PVBS in the previous section, it can be preliminarily determined that the power source of the foldable and self-deployable mechanism comes from the reciprocating linear actuator. On this basis, it is thought to use the crank-slider structure [18] to convert the linear motion into rotational motion to realize the machine arm's folding and deployment finally.

The composition of the arm foldable and self-deployable mechanism can be seen in Fig. 6 **d**, in which the drive base realizes the semi-linkage between the opening and closing of the arm and the PVBS. Fig. 6 also shows three forms of work. Fig.6 **a** shows Nezha-F working in the air and entering the water. When the vehicle falls from the air to the water surface in the form of a quadrotor, the piston is at the position of maximum buoyancy, and the entire foldable mechanism is fully unfolded. The 3D printed structure in the red circle limits the further rise of the machine arm under the action of the propeller thrust. When performing underwater tasks, the float needs to reduce its buoyancy. At this time, under the action of the torsion spring, the whole arm is gradually retracted with the downward movement of the piston, as shown in Fig. 6 **b**. The opening and closing angle of the arm before full retraction is affected by the position of the piston. Therefore, this interval is called the linkage area. When the piston moves further down, it reaches the free movement area, and the transmission base is limited by the edge of the buoyancy cylinder (as shown by the red circle) and will not move further with the piston, as shown in Fig. 6 **c**. This means that the movement of the piston in the free area does not affect the streamlined shape of the vehicle underwater. The process is reversed when the vehicle completes its underwater mission and needs to be recovered.

In order to further determine the length parameters of each part of the folding structure of the machine arm, the simplified schematic diagram shown in Fig. 7 is used for

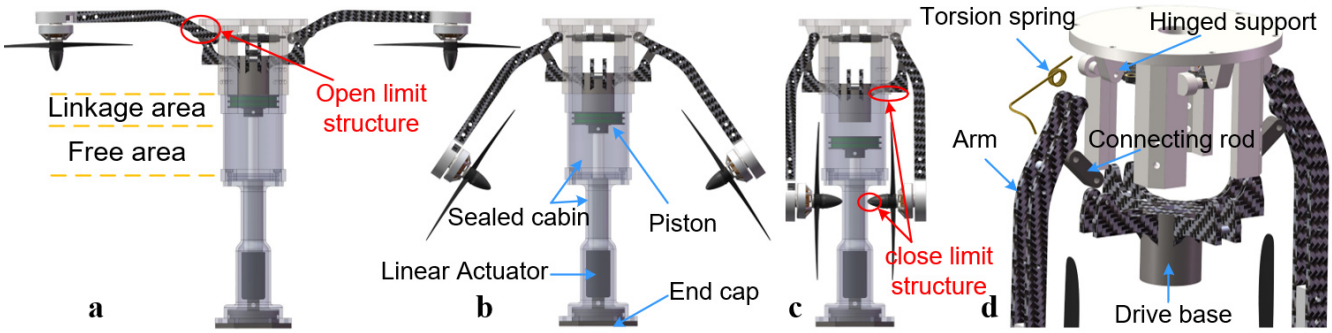

Fig. 6. Arm foldable and self-deployable mechanism and PVBS cooperation process diagram.

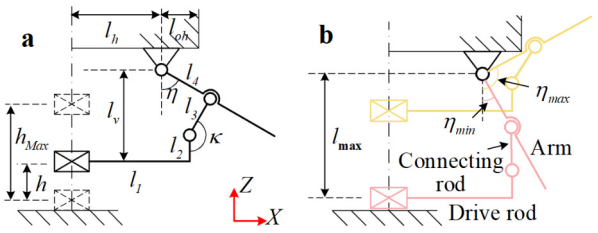

Fig. 7. Simplified picture of arm folding mechanism. **a** contains some important parameters. **b** shows two extreme states.

analysis. The expression for the angle of rotation η can be calculated by the law of cosines:

$$\eta = \arccos\left[\frac{(l_{h'})^2+l_3^2+2l_3\,(l_{h'})\times\sin\kappa-l_4^2-(l_v)^2}{-2l_4l_v}\right] \quad (1)$$

$$\kappa = \frac{3}{2}\pi-\arctan\left(\frac{l_v}{l_{h'}}\right)-\arccos\left[\frac{l_3^2+l_v^2+(l_{h'})^2-l_4^2}{2l_3\sqrt{l_v^2+(l_{h'})^2}}\right] \quad (2)$$

Where $l_{h'}=l_1-l_h$, $l_v=l_{\max}-h-l_2$. When h is equal to 0, the arm is fully retracted and η is the smallest. On the contrary, when h is the largest, η also reaches the largest. In order to smoothly realize the opening and closing of the arm, the effective rotation angle range ($\eta_r=\eta_{max}-\eta_{min}$) of the arm should be as large as possible and at least 90°.

The effective distance of the linear actuator is 50mm. Take h_{Max}=24mm as the actuating distance of the drive arm deployment, which means that the piston still has 26mm free movement space to adjust the buoyancy force underwater after the arm is completely closed. In addition, according to the size of the four-in-one ESC to be placed, determine l_h=32.5mm, and determine l_{oh}=12.5mm by the diameter of the electronic compartment and the position of the hinge point. In order to meet the coordination and compactness of the overall structure, let $l_{\max}$=39mm, l_1=37.5mm, l_2=15mm.

To avoid singularities, the following constraints also need to be met:

$$(l_{v\max}-l_2-l_3)^2+(l_1-l_h)^2<l_4^2 \quad (3)$$

$$(l_2-l_v)^2+(l_1-l_h)^2+l_3^2>l_4^2 \quad (4)$$

Finally, we choose l_3=15mm, l_4=15mm, so that η_r=200.29°. Due to the existence of the limit mechanism, η still needs to be satisfied $\eta<\pi/2+\arccos(l_{oh}/l_4)$, so finally η_r=104.08°, of which 14.08° is the redundant angle that exists to avoid singularity at η_{min}.

C. Avionics

The electronic bin adopts an acrylic cylinder with an inner diameter of 83mm and a thickness of 2mm as the main pressure-resistant shell. The inside of the electronic bin is used to place most of the circuits that need to be waterproof. The electronic bin constitutes 44 percent of the overall weight. The electronic system consists of the control module, drive module, power supply module, communication module, and various sensors.

The control module is composed of two micro control units. The pixhawk4 mini flight control is mainly responsible

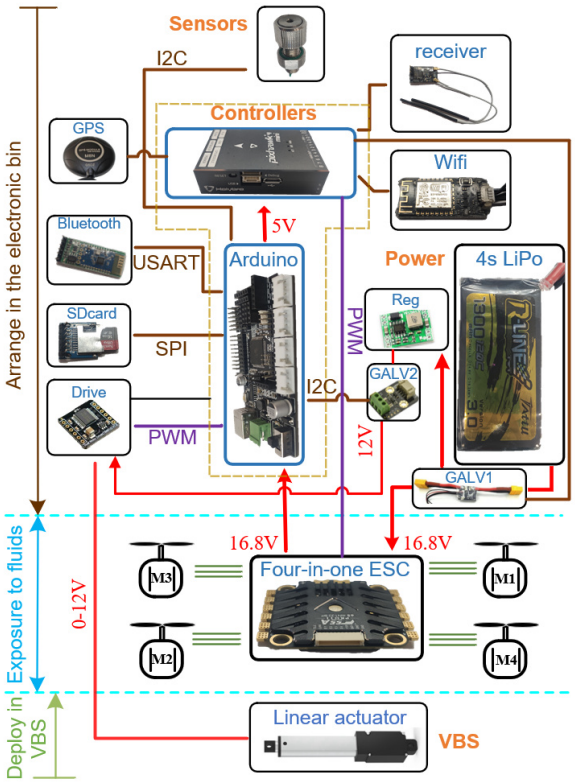

Fig. 8. Simplified picture of arm folding mechanism. **a** contains some important parameters. **b** shows two extreme states.

for the vehicle's cross-media and air cruise process. It has built-in attitude sensors and rich communication interfaces. The Arduino control board is used to switch the underwater working mode and control the PVBS. It also integrates a temperature-depth sensor for measuring underwater environmental parameters and acquiring depth state variables, an SD card module for underwater data storage, and a full-duplex Bluetooth module for program burning.

The drive unit used in the air is a four-in-one ESC. This module generates serious heat when working, so it was directly exposed to the medium after being sealed with epoxy. The drive of the underwater PVBS is placed in the electronic compartment. The clock register used by the Arduino to control the PWM is 8 bits, and the PWM is 255 when the duty cycle is 100%.

The battery system consists of a lithium battery with 4s 1300mah 120C, which is directly connected to the ESC. In addition, a step-down module is connected in parallel to reduce the voltage to 12V, which acts on the underwater drive module. The power of the float to perform underwater tasks is small, and the GALV1 cannot meet the measurement requirements. Thus, a small-range GALV2 is added between the step-down module and the underwater drive to measure the underwater power consumption. The Arduino is powered by the source voltage output of the ESC, and the flight controller is powered by the 5V voltage regulator interface on the Arduino. The rest of the modules are provided by the onboard 5V voltage of the Arduino or flight controller board. The specific connection method and communication

protocol can be seen in Fig. 8. Other detailed parameters of Nezha-F can be found in Table II. The coefficient of drag is calculated by Fluent. The medium of the computational domain is fresh water (1g/cm3), and the working condition is 0.1m/s.

TABLE II
DESIGN PARAMETERS

Description	Value
Mass	1.25kg
Coefficient of drag (close/open arm)	0.56 / 0.81
Piston radius	21 mm
Underwater endurance	29.54h
Maximum variable volume/weight	69.2 cm3 / 69.2∼71.2g
Maximum diving depth	8.5m
Propeller size	6 inches
Motor KV	2000 rpm/V
Air endurance	4min 41s

III. DYNAMICS AND CONTROL

The method of aerial modeling is consistent with that of [19,20] and will not be repeated here. This section only focuses on the underwater motion modeling of Nezha-F, the modeling compensation process of linear actuators, and the control methods used in practical experiments.

A. Underwater Motion Modeling

Nezha-F works in shallow water, so the variation of water density and the effect of different water depths on shell compression are ignored in the modeling process. The dynamic model of Nezha-F underwater is as follows:

$$m\ddot{z} = mg - \rho_{\text{water}}\ (V_0 + \Delta V)\, g - \frac{1}{2} C_{dz} \rho_{\text{water}}\ A\dot{z}|\dot{z}| \quad (5)$$

$\Delta V = \int_0^t S v_b(t) dt$ is the cumulative change in volume, where $v_b(t)$ is the speed of the linear actuator, also considered as an input to the underwater control system. S is the cross-sectional area of the piston. m is vehicle mass. V_0 is the initial volume. ρ_{water} is the density of water. C_{dz} is the vertical resistance coefficient of the vehicle in the water. A is the projected area of the vehicle in the z-direction.

B. Actuator Modeling

Ideally, the model of the actuator should be linear. However, in practice, it is usually nonlinear due to the influence of varying pressure. This nonlinear characteristic will deteriorate the control effect. In order to determine the characteristics of the actuator in this paper, the time of the actuator being pushed from the minimum position to the maximum position and the reverse process at different depths and different PWMs were tested. The duty ratio of PWMs selected in the experiment are 100%, 80%, 60%, 41%, and 21%, respectively, and the depths are 0m, 2.4m, 4.4m, 6.4m, and 8.4m, respectively. Each data point is the average of three repeated experiments. For markup purposes, define the process of linear actuator extension as open and the opposite as close in Fig. 10. The missing experimental data points in the 5 sets of experiments with the arm opening represent that the complete arm opening action cannot be completed under the corresponding PWM.

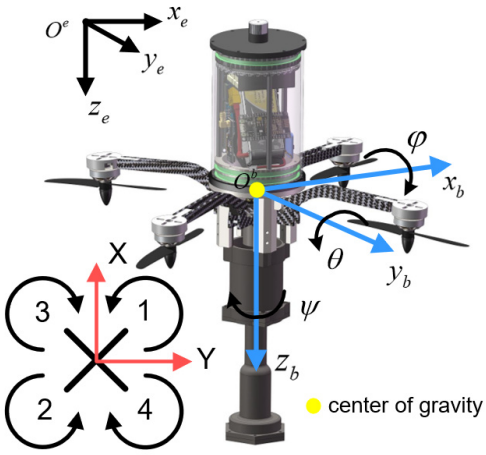

Fig. 9. coordinate systems and obverse directions of Nezha-F.

It can be seen from Fig. 10 that in the process of arm closing, the time required decreases slowly with the increase of depth. In the process of arm opening, the deeper the depth is, the more time it takes to fully expand under the same PWM, and the greater the PWM that meets the minimum expansion requirement. Through the above experiments, it is not difficult to find that the push rod used to adjust the buoyancy is an obvious nonlinear actuator, the mechanism has obvious dead zone asymmetry, and the asymmetry difference is more obvious with the increase of depth.

The overall solution is to: first, fit the data points obtained from the pre-experiment. Obtain mathematical expressions of time with respect to depth and PWM in the opening and closing process. It can be seen in Fig. 10 that the curves of closing time at each depth are similar, so the approximate closing time is independent of the depth. Through the least squares fitting, the relationship between the closing time and PWM can be obtained as:

$$C_{\text{time}}\ (PWM) = 6608 PWM^{-1.251} + 6.668 \quad (6)$$

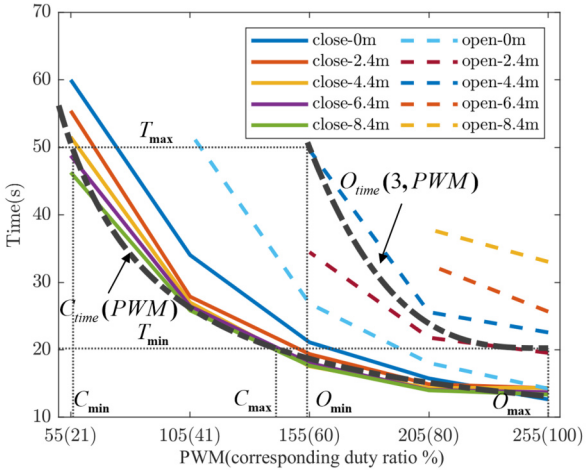

Fig. 10. Experimental data of variable buoyancy system at different depths and PWM. $C_{\text{time}}\ (PWM)$ is the fitted curve for the retraction process of the linear actuator. $O_{\text{time}}\ (3, PWM)$ is the fitted curve for the linear actuator extension at 3m.

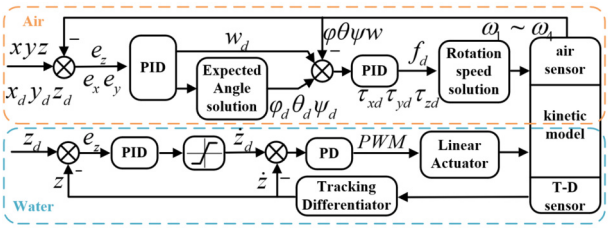

Fig. 11. Schematic diagram of control framework

The opening time is obviously affected by both depth and PWM. The corresponding function can be obtained by similar processing and is expressed in the following form:

$$O_{\text{time}}\,(d, PWM) = f(d)(255 - PWM)^{g(d)} + k(d) \quad (7)$$

Where,

$$f(d) = 8.854e^{-6}\sin(d) + 5.808e^{-7}\left((d-10)^2\right) - 3.007e^{-6} \quad (8)$$

$$g(d) = 0.06226d^{1.819} + 2.564 \quad (9)$$

$$k(d) = 14.7871 + 1.6631d + 0.0527d^2 \quad (10)$$

Then, the task time of more than 50s is regarded as a situation that the task cannot be completed, that is, $T_{\max}$ =50. After setting $O_{\max}$=255, the corresponding depth can be brought into equation (4) to obtain $T_{\min}$. In $[T_{\min}, T_{\max}]$, the opening and closing process of the actuator is symmetrical in time. Therefore, mapping the original PWM calculated by the controller to the interval range of $[T_{\min}, T_{\max}]$ preliminarily solves the problem of the asymmetry of the dead zone of the actuator. Finally, the revised PWM can be obtained by substituting the corresponding mapping value of the previous step into (6) or (7). This process solves the problem of actuator nonlinearity.

It should be noted that the minimum expansion time of the linear actuator increases with depth and cannot be reduced by compensation. Therefore, the method in this paper ensures that the input PWM and response time of the actuator are optimally linearized at a certain depth. The actuator performance is still somewhat nonlinear with increasing depth. However, this has a small impact on the final control effect, as demonstrated in the final field experimental results.

C. Control Strategy

The vehicle control strategy also consists of two parts: underwater and above water. As shown in Fig. 11, the control strategy in the blue box is the underwater control strategy, and the control strategy in the orange box is the control strategy during the water exit process and in the air.

When underwater, Nezha-F only relies on the depth information measured by the temperature-depth sensor as a known state. The speed information is obtained by processing the known depth information through the differential tracker to avoid amplifying the noise after the PID differential segment. Through the PID of the outer loop, the depth error can be mapped to the corresponding target velocity information, and the limiter module can ensure that the maximum speed of the vehicle does not exceed a certain value. Finally, through the PD control of the inner loop, the corresponding PWM value is output to control the pushing speed of the linear actuator and realize the function that the vehicle ascent or dives at a certain speed and can maintain a certain depth for a long time.

The structure of double closed-loop PID is also used during water crossing and air missions. The initial input is the position coordinates of the target. After passing through the PID of the outer loop, the target speed of the z-axis in the body coordinate system and the three target rotation angles of the body are obtained. The target yaw angle is 0 by default, and the target pitch angle and roll angle are obtained through the inverse solution of the dynamic equation of the quadrotor. Then through the PID controller of the inner loop, the thrust of the propeller target and the control torque of the three targets are obtained, and the rotational speed of each propeller motor is obtained through the thrust distribution equation and the motor model of the propeller.

IV. SIMULATIONS AND EXPERIMENTS

A. Full-mission Experiments

The experiment was completed in Qiandao Lake, Zhejiang Province, China. The entire mission process includes take-off from shore, performing aerial missions, entering water and performing underwater missions, exiting-entry-exiting water tests, and returning to shore. The experimental data and images can be seen in Fig. 12. During the air mission Nezha-F takes off to a relative altitude of 5m and then tracks the four pre-defined target points (①, ②, ③, ④ in a square with a 10m side in top view). ① to ③ remains at an altitude of 5m and gradually decreases in altitude on the path from ③ to ④, eventually entering the water at ④. During the take-off and air mission phases, it can be seen from picture **A** in Fig. 12 that the aircraft's flight attitude is stable, and the maximum angle of the drone does not exceed 15.4°. The GPS curve in Fig. 12 **a** also shows that the flight path is very smooth.

When Nezha-F enters the water, the depth-keeping task is performed sequentially at 1m, 3m, 6m, 5m, and 3m underwater, as shown in **B1**. The mission time corresponding to each target depth is the 90s. The final results show no overshoot or steady state errors at any depth. And the dynamic performance of each depth in the descending process is consistent with the ascending process. It is worth noting that there is a large deviation between the actual curve and the simulation results in the time of 350-400s. This is because the state of the arm appears to have a certain opening in the ascent stage, which leads to an increase in the water damping coefficient and the speed unable to reach the predetermined 0.1m/s (see 350-400s of **B2**). The depth-keeping effect of Nezha-F in all other stages is consistent with the simulation results, which also reflects the effectiveness of the compensation for the actuator.

When floating on the surface, the vehicle is affected by the waves, and its attitude angle oscillates in the range of -6.6°-2.1°. Then, the test of exiting-entry-exiting water was carried out, in which the initial attitude was not conducive to water exit during the first water-out process, so 0.5-6.5s

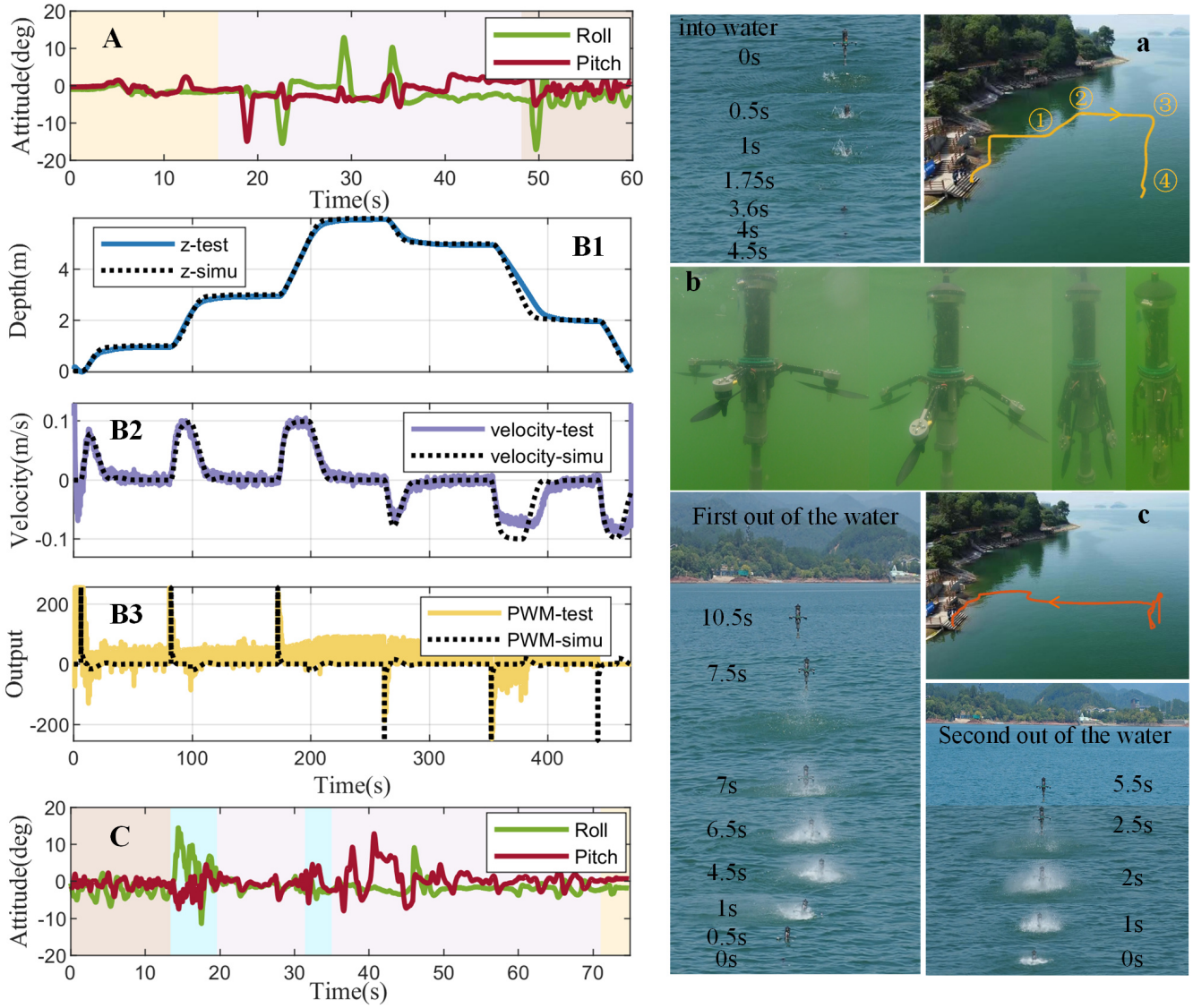

Fig. 12. Full-mission experiment. **A**: The process of taking off, performing an aerial mission, and merging into water. **B1,2,3**: underwater depth determination mission, where **B3** is the output before correction. **C**: The two exits from the water surface and the subsequent return process. **a**, **b** and **c** are the experimental diagrams corresponding to **A**, **B** and **C** respectively. In the **A/C** diagram, orange represents take-off/landing, purple represents performing aerial missions, yellow represents floating on the water surface, and blue represents the process of exiting the water. The three zero-second moments in the graph on the right correspond to real times of 44.5s, 13.4s, and 31.4s respectively.

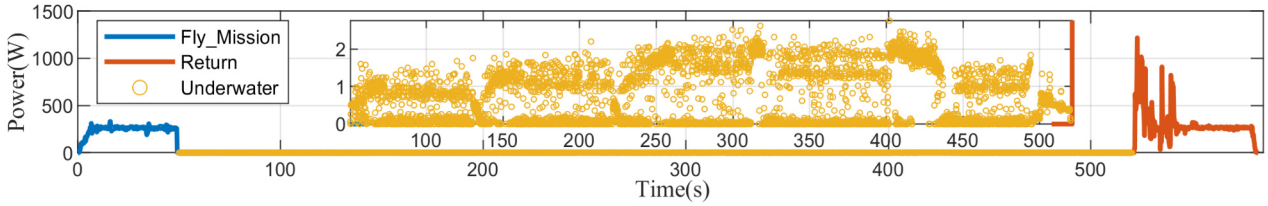

Fig. 13. Power consumption of the whole process experiment

was the stage of adjusting the attitude on the water surface, and the water was completed in the following 2.5s. More stable attitude during the second water exit. And it takes 2.5s to complete the water exit task. The maximum attitude angle of the water exit process does not exceed 14.48°. Finally, Nezha-F returned at an altitude of 3m, and when approaching the landing point, it rose to 5m and landed, ending all missions.

B. Power Analysis

1) Full-mission Power Consumption: It can be seen in Fig. 13 that the flight power is relatively constant at an average of 265W during the execution of the aerial mission and the return phase. The power consumption increased by an average of 136% during the two water exits processes. This results from the collision between the propeller and

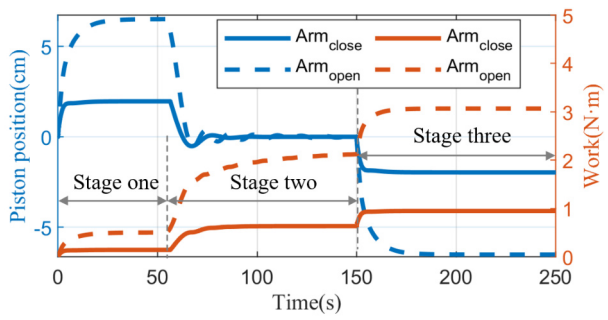

Fig. 14. Theoretical analysis of arm foldable structure to reduce power consumption during 6m underwater depth-keeping task.

the water surface, causing the motor speed to drop, and the motor still has to maintain a high speed. Compared with the air, the power consumption underwater is extremely low. It can also be seen in the enlarged scatter diagram that the power consumption increases with the depth in the process of descending and fixing the depth, and the corresponding power consumption is 34.9J, 52.90J, and 71.29J, respectively. In the ascending stage, the push rod needs to overcome the water pressure to do work. The power consumption is higher, 62.68J, and 77.02J, respectively.

2) Underwater Power Consumption Analysis: The work done by the PVBS under ideal conditions can be expressed as (11).

$$W = \int_0^t \left[\rho_{\text{water}}\, gzS + \left(\frac{\Delta V}{V} PS \right) + F_f \right] dz \qquad (11)$$

Where the right-hand side of (11) from the left is the work done to overcome the water pressure, the work done to overcome the negative pressure in the bin, and the work done to overcome the sliding friction, respectively. V is the initial volume of air in the sealed chamber, F_f is the sliding friction between the piston and the VBS. Based on this, we compared the vehicle's power consumption when performing a 6m depth-keeping task with the arm fully deployed and fully folded. It can be seen from Fig. 14 that the energy consumption is roughly divided into three stages-Stage one: from surface to dive at 0.1m/s, Stage two: slow down and finally keep depth at 6m, and Stage three: ascent from 6m at 0.1m/s. Finally, according to Fig. 14, when performing the same task, the vehicle's power consumption with the arm fully deployed is theoretically 3.24 times that with the arm fully folded. And the overall moving distance of the push rod is 2.43 times. This indicates that the proposed HAUV has the advantage of lower power consumption underwater than the traditional multi-rotor HAUV.

V. CONCLUSION

In this paper, a small HAUV(Nezha-F) based on PVBS is proposed, aiming to solve the problem of excessive damping of most current HUAVs with multi-rotor configuration underwater. The self-foldable and deployable of the Nezha-F's arm was achieved by combining a special crank-slider structure with the PVBS. Additionally, the dynamic performance degradation of the used small linear actuators with increasing depth is experimentally analyzed. The corresponding solutions in terms of control are also proposed. Finally, the ability of Nezha-F to perform a full mission and the detailed power consumption of each stage were verified through practical experiments.

In the future, we plan to conduct further research on the timing of HAUV water-exit under wave interference.

REFERENCES

[1] Z. Zeng, C. Lyu, Y. Bi, Y. Jin, D. Lu, and L. Lian, "Review of hybrid aerial underwater vehicle: Cross-domain mobility and transitions control," *Ocean Eng.*, vol. 248, 2022.

[2] W. Weisler, W. Stewart, M. B. Anderson, K. J. Peters, A. Gopalarathnam, and M. Bryant, "Testing and Characterization of a Fixed Wing Cross-Domain Unmanned Vehicle Operating in Aerial and Underwater Environments," *IEEE J. Oceanic Eng.*, vol. 43, no. 4, pp. 969-982, 2018.

[3] D. Lu *et al.*, "Design, fabrication, and characterization of a multimodal hybrid aerial underwater vehicle," *Ocean Eng.*, vol. 219, 2021.

[4] Y. H. Tan and B. M. Chen, "A Morphable Aerial-Aquatic Quadrotor with Coupled Symmetric Thrust Vectoring," in *2020 IEEE International Conference on Robotics and Automation (ICRA)*. 2020, pp. 2223-2229.

[5] Y. Bi, Y. Jin, C. Lyu, Z. Zeng, and L. Lian, "Nezha-Mini: Design and Locomotion of a Miniature Low-Cost Hybrid Aerial Underwater Vehicle," *IEEE Robot. Autom. Lett.*, vol. 7, no. 3, pp. 6669-6676, 2022.

[6] Z. Li, Y. Liu, F. Guo, G. Xue, S. Li, and X. Li, "Multi-objective optimization of the shell in autonomous intelligent argo profiling float," *Ocean Eng.*, vol. 187, 2019.

[7] E. Gokbel and S. Ersoy, "Launchable rotary wing UAV designs and launch mechanism designs for rotary wing UAV," *Journal of Mechatronics and Artificial Intelligence in Engineering*, vol. 2, no. 2, pp. 102-113, 2021.

[8] D. Falanga, K. Kleber, S. Mintchev, D. Floreano, and D. Scaramuzza, "The Foldable Drone: A Morphing Quadrotor That Can Squeeze and Fly," *IEEE Robot. Autom. Lett.*, vol. 4, no. 2, pp. 209-216, 2019.

[9] A. Bouman et al., "Design and Autonomous Stabilization of a Ballistically-Launched Multirotor," in *2020 IEEE International Conference on Robotics and Automation (ICRA)*, 2020, pp. 8511-8517.

[10] L. Henderson, T. Glaser, and F. Kuester, "Towards bio-inspired structural design of a 3D printable, ballistically deployable, multi-rotor UAV," in *2017 IEEE Aerospace Conference*, 2017, pp. 1-7.

[11] A. Fabian, Y. Feng, E. Swartz, and D. Thurmer, "Hybrid Aerial Underwater Vehicle (MIT Lincoln Lab)," 2012.

[12] Rockenbauer, Friedrich M., et al. "Dipper: A Dynamically Transitioning Aerial-Aquatic Unmanned Vehicle." *Robotics: Science and Systems*. 2021.

[13] Y. Gao, H. Zhang, H. Yang, S. Tan, T. A. Gulliver, and T. Lu, "Trans-Domain Amphibious Unmanned Platform Based on Coaxial Counter-Propellers: Design and Experimental Validation," *IEEE Access*, vol. 9, pp. 149433-149446, 2021.

[14] R. N. Smith and V. T. Huynh, "Controlling Buoyancy-Driven Profiling Floats for Applications in Ocean Observation," *IEEE J. Oceanic Eng.*, vol. 39, no. 3, pp. 571-586, 2014.

[15] Y. Bai, R. Hu, Y. Bi, C. Liu, Z. Zeng, and L. Lian, "Design and Depth Control of a Buoyancy-Driven Profiling Float," *Sensors*, vol. 22, no. 7, 2022.

[16] V. Viswanathan and T. Taher, "Buoyancy driven autonomous profiling float for shallow waters," in *OCEANS 2016 MTS/IEEE Monterey*. 2016, pp. 1-6.

[17] H. Alzu'bi, I. Mansour, and O. Rawashdeh, "Loon copter: Implementation of a hybrid unmanned aquatic–aerial quadcopter with active buoyancy control," *J. Field Robot*, vol. 35, no. 5, pp. 764-778, 2018.

[18] L. Bai et al., "Design and Experiment of a Deformable Bird-inspired UAV Perching Mechanism," *J Bionic Eng*, vol. 18, no. 6, pp. 1304-1316, 2021.

[19] P. L. Drews, A. A. Neto, and M. F. Campos, "Hybrid unmanned aerial underwater vehicle: Modeling and simulation," in *2014 IEEE/RSJ International Conference on Intelligent Robots and Systems*, 2014, pp. 4637-4642.

[20] D. A. M. Ravell, M. M. Maia, and F. J. Diez, "Modeling and control of unmanned aerial/underwater vehicles using hybrid control," *Control. Eng. Pract.*, vol. 76, pp. 112-122, 2018.